Fully Printable Mesoscopic Perovskite Solar Cells with Organic Silane Self-Assembled Monolayer

Linfeng Liu, Anyi Mei, Tongfa Liu, Pei Jiang, Yusong Sheng, Lijun Zhang, and Hongwei Han*

Michael Grätzel Center for Mesoscopic Solar Cells, Wuhan National Laboratory for Optoelectronics, School of Optical and Electronic Information, Huazhong University of Science and Technology, Wuhan, Hubei 430074, P.R. China

S *Supporting Information*

ABSTRACT: By the introduction of an organic silane self-assembled monolayer, an interface-engineering approach is demonstrated for hole-conductor-free, fully printable mesoscopic perovskite solar cells based on a carbon counter electrode. The self-assembled silane monolayer is incorporated between the TiO_2 and $CH_3NH_3PbI_3$, resulting in optimized interface band alignments and enhanced charge lifetime. The average power conversion efficiency is improved from 9.6% to 11.7%, with a highest efficiency of 12.7%, for this low-cost perovskite solar cell.

Most recently, organic lead halide perovskite has attracted considerable attention as a prominent light harvester in solar cells because of its excellent properties and innovative device design.[1−4] To utilize this magic material, multiple research groups have demonstrated various device architectures,[5−8] among which mesoscopic $TiO_2/CH_3NH_3PbI_3$ solar cells, especially those avoiding the use of hole-transporting materials (HTMs),[6,9] have drawn increased interest from the photovoltaic community because high-cost HTMs are not required and the manufacturing process is much simpler. After Etgar et al.[6] first reported HTM-free mesoscopic $TiO_2/CH_3NH_3PbI_3$ solar cells with a power conversion efficiency (PCE) of 5.5%, an efficiency of 8.04% was obtained using a modified $CH_3NH_3PbI_3$ spin-coating method,[10] which was further improved to 10.85% with a two-step deposition method.[11] Although these kinds of architectures do not require high-cost HTMs, they still need Au counter electrodes (CEs) formed by thermal evaporation, which is a highly energy-consumptive and complicated process. To reduce the cell fabrication cost caused by HTMs and Au CEs at the same time, we have developed hole-conductor-free mesoscopic $TiO_2/CH_3NH_3PbI_3$ perovskite solar cells with low-cost carbon CEs. By the use of one-step drop-coating deposition to infiltrate $CH_3NH_3PbI_3$ through screen-printed carbon/ZrO_2/TiO_2 films, an initial PCE of 6.64% was achieved.[12] This performance was further improved by optimization of the mesoporous carbon contact[13,14] and TiO_2 scaffold.[15] Recently, a high PCE exceeding 12% was obtained in carbon-based devices using a sequential solution deposition method,[16] and moreover, high stability (over 1000 h) of this fully printable, hole-conductor-free perovskite solar cell was achieved.[9] Although the efficiency was still inferior to that of cells using HTMs and Au metal, the architecture design and outstanding stability indicated very promising prospects for low-cost photovoltaic technology,

encouraging us to further optimize this low-cost fully printable mesoscopic perovskite solar cell.

As a crucial component of mesoscopic perovskite solar cells, the TiO_2 layer acts as a selective contact to extract electrons as well as a scaffold to sustain the perovskite, which influences the device performance significantly. It was demonstrated that the high chemical capacitance of TiO_2 under illumination may prevent the quasi-Fermi level of electrons from rising high enough for any given charge density,[17] hence decreasing the photovoltage of perovskite solar cells. To suppress this decrease, Al_2O_3 and ZrO_2 scaffolds with fewer surface and sub-band-gap states were successfully used.[18] On the other side, in dye-sensitized solar cells (DSSCs), surface modification of porous TiO_2 is well-known as an effective method to passivate the TiO_2 surface, blocking electron recombination from TiO_2 to the electrolyte (or hole conductor). With this motivation, an inorganic Sb_2S_3 layer was inserted at the interface between TiO_2 and $CH_3NH_3PbI_3$ perovskite to block the charge recombination process and the photocatalytic effect of TiO_2,[19] while an organic $HOCORNH_3^+I^-$ anchor was introduced between the TiO_2 surface and the perovskite to tune the perovskite crystal growth and retard charge recombination.[20] Also, a covalently bonded strong silane monomolecular layer has been used to decrease the electron back-transfer on the TiO_2 surface in conventional DSSCs[21] and to tune the conduction band, surface energy, and wetting properties of metal oxides.[22,23] In addition, theoretical studies have shown that the interface electronic structure and passivation are crucial for perovskite solar cell performance,[24,25] indicating potential profit from TiO_2 surface modification. In this work, we inserted an organic silane self-assembled monolayer (SAM) between TiO_2 and $CH_3NH_3PbI_3$ in hole-conductor-free mesoscopic TiO_2/$CH_3NH_3PbI_3$ solar cells based on carbon CEs and assessed the effect of this silane layer on the interface properties by means of electrochemical and photoluminescence (PL) measurements.

Fully printable hole-conductor-free mesoscopic perovskite solar cells were fabricated by the following process. FTO glass was patterned using Zn and 2 M HCl(aq) before use. After the glass substrate was cleaned successively with deionized water, ethanol, and acetone using an ultrasonic bath for 15 min, a compact TiO_2 layer was prepared by aerosol spray pyrolysis deposition of a solution of titanium diisopropoxide bis-(acetylacetonate) in ethanol onto the glass substrate. Then a 2 μm porous TiO_2 layer, a 1 μm ZrO_2 spacer layer, and a 9 μm

A

carbon CE were screen-printed on the substrate layer by layer. The TiO_2 layer was sintered at 500 °C for 30 min, and the ZrO_2 and carbon layers were sintered at 400 °C for 30 min. The porous films were immersed in a 0.05 mM solution of amino-propyltrimethoxysilane in 2-propanol for several hours to introduce a silane layer on the TiO_2 surface, and then the films were rinsed copiously in 2-propanol and dried under a flow of N_2. The perovskite $CH_3NH_3PbI_3$ was deposited into the porous films by a two-step sequential method. First, 1.5 μL of 1 M PbI_2 in DMF was infiltrated into the films by drop-coating, followed by annealing at 70 °C for 30 min. After that, the films coated with PbI_2 were dipped in a 10 mg/mL solution of CH_3NH_3I in 2-propanol for about 12 min. After the films turned dark brown, indicating the formation of $CH_3NH_3PbI_3$, they were rinsed with 2-propanol.

The structure of a typical hole-conductor-free mesoscopic perovskite solar cell based on a carbon CE is shown in Figure 1a.
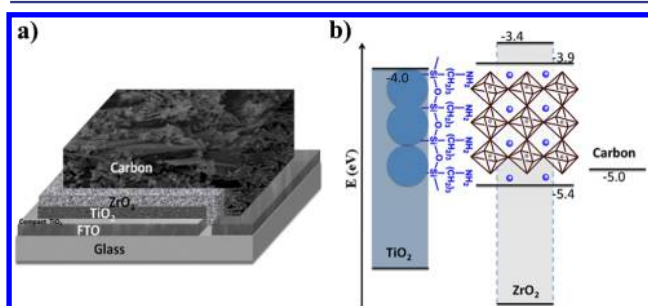
Figure 1. (a) Structure of the fully printable mesoscopic perovskite solar cell based on a carbon CE. (b) Energy band diagram of the device and the organic silane SAM between the TiO_2 surface and the perovskite.

All of the films, including the nanoporous TiO_2 layer, ZrO_2 insulating layer, and mesoscopic carbon CE, were screen-printed onto the FTO glass substrate layer by layer. The energy levels (Figure 1b) allow electron extraction from $CH_3NH_3PbI_3$ (−3.9 eV) to the TiO_2 conduction band (−4.0 eV) and hole collection from the $CH_3NH_3PbI_3$ valence band (−5.4 eV) to the carbon CE (−5.0 eV); the silane SAM located between the TiO_2 surface and the perovskite will be discussed later. Figure S1 in the Supporting Information (SI) shows a representative scanning electron microscopy (SEM) image of a cross section of the monolithic device. The carbon CE layer can be clearly distinguished from the sublayers, and the ZrO_2 layer functions as a spacer to prevent any direct contact between carbon CE and the TiO_2 film.

Actually, the assembly of the silane monolayer onto the TiO_2 surface can be realized by the formation of covalent bonds through condensation reactions between the hydrolyzed silane alkoxy groups and hydroxyl groups present at the TiO_2 surface. The ATR-FTIR spectrum was measured to specify the formation of the silane SAM (Figure 2). TiO_2 film samples functionalized with silane SAMs using different times are characterized by the presence of a broad band in the 3800−3000 cm^{-1} region, and the absorption bands at 2929 and 2976 cm^{-1} can be assigned to the asymmetric and symmetric stretches of −CH_2 groups on the alkyl chains. The absorption bands in the low-frequency region can be assigned to the bending modes of −NH_2 groups (1627 and 1582 cm^{-1}), −CH_2 groups (1410 cm^{-1}), and the Si−O−Si (1066 cm^{-1}) network. The intensities of the −NH_2 and −CH_2 bands increase with increasing treatment time up to 24 h. These results indicate that the silane SAM was successfully introduced onto the TiO_2 surface.
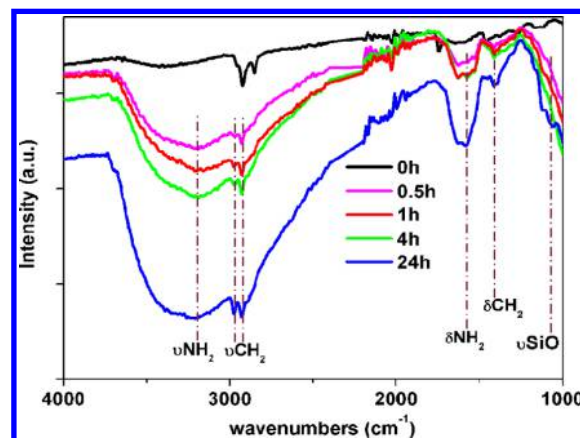
Figure 2. FTIR spectra of TiO_2 films modified with silane SAMs using different treatment times.

Devices obtained using different silane treatment times were fabricated with the modified two-step sequential method to investigate the effect of the extent of TiO_2 surface coverage. The characteristic parameters are summarized in Table S1 in the SI. Compared with an unsilanized cell, silane-treated cells show increased open-circuit photovoltage (V_{OC}) with extended immersion time in silane solution, while the short-circuit photocurrent density (J_{SC}) and PCE reach maximum values at around 1−4 h. It can be observed that the fill factor (FF) decreases to the previous value of 0.69 with 24 h of treatment after reaching over 0.75 at the best performance point.

SEM was used to investigate the significant difference in device performance resulting from the silane SAM. Figure 3 shows typical SEM top-view images of a TiO_2 film filled with spin-coated perovskite at different treatment times, where a high spin rate was applied to avoid any capping layer with excess perovskite. The amount of $CH_3NH_3PbI_3$ loaded on the silane-SAM-modified TiO_2 (Figure 3e,f) is apparently larger and more compact than on the unmodified surface (Figure 3c,d). Indeed, compared with deposition of $CH_3NH_3PbI_3$ on the unmodified TiO_2 surface, stronger UV−vis absorption was found using silane SAM modified TiO_2 (Figure S2). This phenomenon is probably due to the enhanced affinity between these two layers induced by the reported hydrogen-bonding or electrostatic interactions between the amino groups and the perovskite framework.[26] Herein it would benefit the precursor to wet the TiO_2 surface and infiltrate into the porous TiO_2 when dropped and to remain in the pore during the subsequent high-speed spin process and dipping process in CH_3NH_3I/propanol solution.

Interestingly, when the treatment time was 24 h, a hill-shaped accumulation of perovskite close to the surface can be observed (Figure 3h), and also some crystalline perovskite grows out of the TiO_2 pore, forming submicron-sized crystals beyond the surface (Figure 3g). This behavior may be ascribed to excess adsorption of silane on TiO_2 that leads to a multilayer silane network and decreased pore size. Under these conditions, the bottleneck of a TiO_2 mesopore is easily blocked, resulting in unfavorable infiltration of the PbI_2 precursor into the TiO_2. This provides a reasonable explanation for the decrease in J_{SC} upon 24 h treatment to a value even lower than that for the control device. The above results indicate that a proper coverage extent of silane on the porous TiO_2 surface and an appropriate immersion time can be chosen at the concentration of silane solution employed.
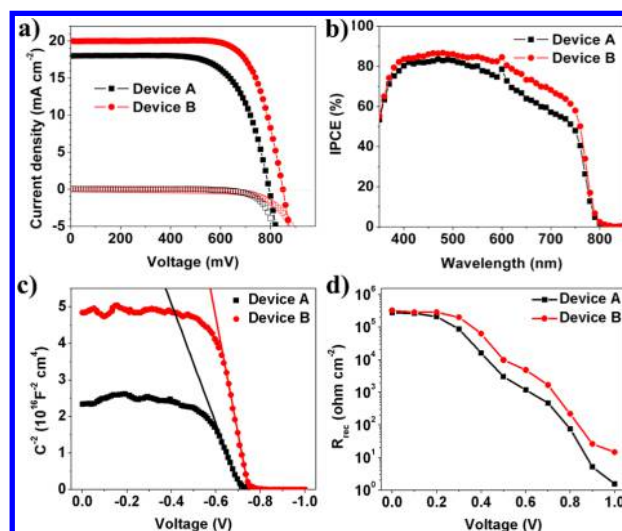
Representative photocurrent density−voltage ($J−V$) curves of the control device (device A) and the silane-SAM-treated device

B
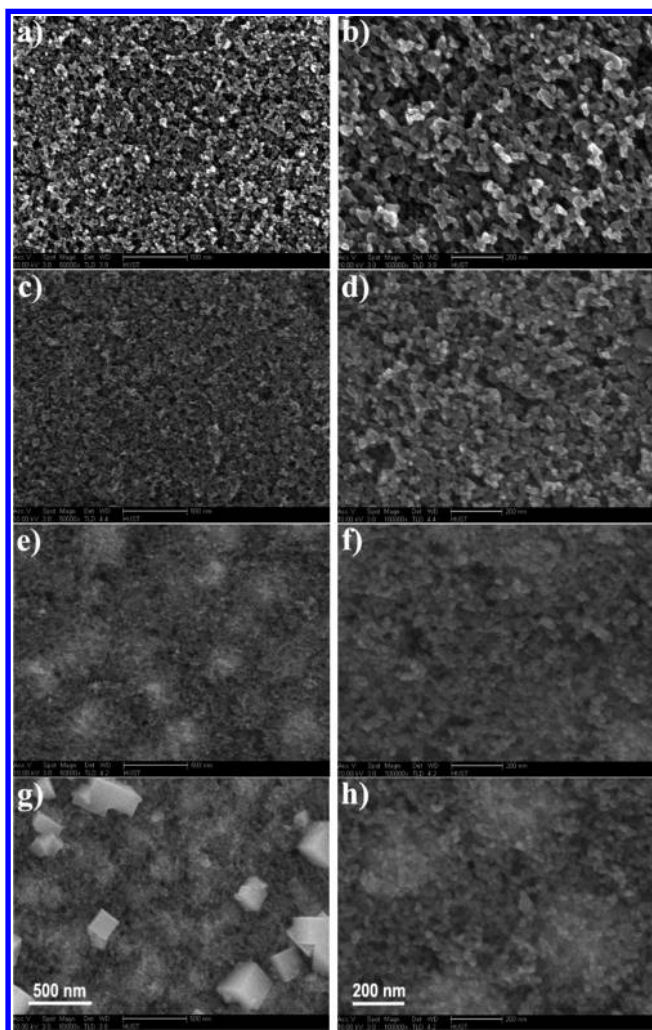
Figure 3. SEM images showing surfaces of (a, b) bare TiO_2 films deposited on FTO glass and (c–h) TiO_2 films filled with $CH_3NH_3PbI_3$ after treatment with silane for (c, d) 0 h, (e, f) 1 h, and (g, h) 24 h. (left) Low-resolution images (scale bar = 500 nm); (right) high-resolution images (scale bar = 200 nm).

Figure 4. (a) Representative $J-V$ curves, (b) IPCE plots, (c) Mott–Schottky analyses, and (d) plots of recombination resistance (R_{rec}) at different applied bias voltages extracted from impedance analysis of mesoscopic perovskite solar cells without (device A) and with (device B) silane SAM.

(device B) are presented in Figure 4a, and the characteristic parameters are given in Table S1. The average photovoltaic performance and error bars (with 10 individuals fabricated to guarantee reliability) are shown in Figure S3. The devices present high reproducibility with the method reported here. At the optimum treatment time of 1 h, an average PCE of 11.7% (max 12.7%) was achieved, which is higher than the average control device efficiency of 9.5% (max 9.9%). Benefiting from the inserted layer, the average V_{OC} increased from 801 mV to around 833 mV, while the average FF increased from 0.67 to 0.72. It can be concluded that the performance is improved all-around with the introduction of the silane SAM between the porous TiO_2 and the crystalline perovskite. In addition to the enhancement in V_{OC} and FF, the average photocurrent is also increased from 17.7 to 19.6 mA/cm^2. The incident photon-to-current conversion efficiency (IPCE) describes the ability of the device to turn incident photons into extracted electrons at a given wavelength. The IPCE of the silane-SAM-based device generally reached a higher value than that of the control device (Figure 4b), in reasonable agreement with the measured photocurrent–voltage curves.

Capacitance–voltage measurements[10,28] were performed to further understand the effect of the inserted organic silane layer. From the x-intercept of the linear regime in the Mott–Schottky plot (Figure 4c), the built-in potential at the $TiO_2/CH_3NH_3PbI_3$ contact can be obtained.[28] The built-in potential of the device with the silane SAM layer is around 37 mV higher than that of the device without this layer. This difference should be attributed to the decreased work function of TiO_2 induced by the surface treatment with terminal electron-donating amine groups, which directs the dipole moment away from the TiO_2 surface.[23,27] A larger built-in potential means an enhanced driving force for the separation of photogenerated carriers and also an extended depletion region for efficient suppression of electrons from TiO_2 to $CH_3NH_3PbI_3$. Therefore, the introduction of the silane SAM between the TiO_2 film and the $CH_3NH_3PbI_3$ layer directly contributes to the output voltage of solar cells. The interfacial recombination resistance (R_{rec}) was determined by electrochemical impedance spectroscopy at an applied voltage with a typical Nyquist plot shown in Figure S4. The R_{rec} values extracted from the fits show slower electron back-transfer in the silane-SAM-based devices (Figure 4d), which explains the enhanced V_{OC}. This result is in good agreement with that obtained from the typical dark-current curves shown in Figure 4a.

To provide deeper insight into the origin of the effect of the inserted organic silane layer, time-resolved PL measurements on perovskite-coated TiO_2 and ZrO_2 were performed to investigate the charge dynamics in these systems. Figure S5 shows the PL decays collected at the peak perovskite emission (765 nm). With the two-step deposition method, the PL lifetime is reduced significantly when the perovskite film forms a contact with TiO_2, indicating efficient charge extraction (Figure S5a). No significant difference in the PL decay liftimes of TiO_2/perovskite (9.14 ns) and TiO_2/SAM/perovskite (8.76 ns) was observed, which may indicate that the electron extraction process is not influenced by the introduction of the silane SAM between the TiO_2 and perovskite. An interesting and unusual observation arises from the comparison of the PL decay lifetimes of ZrO_2/perovskite (16.16 ns) and ZrO_2/SAM/perovskite (43.96 ns), which shows that the PL decay rate decreases when the silane SAM is used.

The longer charge-carrier lifetime observed with the silane SAM indicates a much lower defect concentration, which is beneficial to the hole transport through the ZrO_2 layer before reaching the carbon back contact and herein contributes to higher FF. In addition, for comparison with two-step deposition method, the PL of samples obtained with a one-step method was also measured (Figure S5b). No significant difference in the decay lifetimes for ZrO_2/perovskite (21.74 ns) and ZrO_2/SAM/perovskite (22.04 ns) was observed, in agreement with the previous result that the devices with and without the silane SAM obtained using the one-step method exhibit almost the same $J-V$ performance (Figure S6 and Table S2). This indicates a probable influence of the silane SAM on the perovskite nucleation/growth process.

In summary, an organic silane self-assembled monolayer was inserted between the TiO_2 surface and the perovskite layer in hole-conductor-free solar cells based on carbon counter electrodes. The silane SAM helps tune the interface electronic structure and passivate the recombination process. As a result, a high efficiency of 12.7% was obtained for a TiO_2/SAM/$CH_3NH_3PbI_3$-based mesoscopic solar cell obtained using a sequential deposition method. Surface modification has been shown to be an effective method to improve device performance. These results show promising prospects for hole-conductor-free mesoscopic perovskite solar cells to approach low-cost photovoltaic industrialization.

■ ASSOCIATED CONTENT

Ⓢ Supporting Information

Experimental details and Figures S1−S6. This material is available free of charge via the Internet at http://pubs.acs.org.

■ AUTHOR INFORMATION

Corresponding Author

*hongwei.han@mail.hust.edu.cn

Notes

The authors declare no competing financial interest.

■ ACKNOWLEDGMENTS

■ REFERENCES

(1) Grätzel, M. *Nat. Mater.* **2014**, *13*, 838.

(2) Jung, H. S.; Park, N. G. *Small* **2014**, *11*, 10.

(3) Bisquert, J. *J. Phys. Chem. Lett.* **2013**, *4*, 2597.

(4) Kim, H.-S.; Im, S. H.; Park, N.-G. *J. Phys. Chem. C* **2014**, *118*, 5615.

(5) Docampo, P.; Hanusch, F. C.; Stranks, S. D.; Döblinger, M.; Feckl, J. M.; Ehrensperger, M.; Minar, N. K.; Johnston, M. B.; Snaith, H. J.; Bein, T. *Adv. Energy Mater.* **2014**, DOI: 10.1002/aenm.201400355.

(6) Etgar, L.; Gao, P.; Xue, Z.; Peng, Q.; Chandiran, A. K.; Liu, B.; Nazeeruddin, M. K.; Grätzel, M. *J. Am. Chem. Soc.* **2012**, *134*, 17396.

(7) Im, J. H.; Jang, I. H.; Pellet, N.; Grätzel, M.; Park, N. G. *Nat. Nanotechnol.* **2014**, *9*, 927.

(8) Zhou, H.; Chen, Q.; Li, G.; Luo, S.; Song, T. B.; Duan, H. S.; Hong, Z.; You, J.; Liu, Y.; Yang, Y. *Science* **2014**, *345*, 542.

(9) Mei, A.; Li, X.; Liu, L.; Ku, Z.; Liu, T.; Rong, Y.; Xu, M.; Hu, M.; Chen, J.; Yang, Y.; Grätzel, M.; Han, H. *Science* **2014**, *345*, 295.

(10) Laban, W. A.; Etgar, L. *Energy Environ. Sci.* **2013**, *6*, 3249.

(11) Aharon, S.; Gamliel, S.; Cohen, B. E.; Etgar, L. *Phys. Chem. Chem. Phys.* **2014**, *16*, 10512.

(12) Ku, Z.; Rong, Y.; Xu, M.; Liu, T.; Han, H. *Sci. Rep.* **2013**, *3*, No. 3132.

(13) Xu, M.; Rong, Y.; Ku, Z.; Mei, A.; Liu, T.; Zhang, L.; Li, X.; Han, H. *J. Mater. Chem. A* **2014**, *2*, 8607.

(14) Zhang, L.; Liu, T.; Liu, L.; Hu, M.; Yang, Y.; Mei, A.; Han, H. *J. Mater. Chem. A* **2015**, DOI: 10.1039/c4ta04647a.

(15) Rong, Y.; Ku, Z.; Mei, A.; Liu, T.; Xu, M.; Ko, S.; Li, X.; Han, H. *J. Phys. Chem. Lett.* **2014**, *5*, 2160.

(16) Hu, M.; Liu, L.; Mei, A.; Yang, Y.; Liu, T.; Han, H. *J. Mater. Chem. A* **2014**, *2*, 17115.

(17) Lee, M. M.; Teuscher, J.; Miyasaka, T.; Murakami, T. N.; Snaith, H. J. *Science* **2012**, *338*, 643.

(18) Bi, D.; Moon, S.-J.; Haggman, L.; Boschloo, G.; Yang, L.; Johansson, E. M. J.; Nazeeruddin, M. K.; Grätzel, M.; Hagfeldt, A. *RSC Adv.* **2013**, *3*, 18762.

(19) Ito, S.; Tanaka, S.; Manabe, K.; Nishino, H. *J. Phys. Chem. C* **2014**, *118*, 16995.

(20) Ogomi, Y.; Morita, A.; Tsukamoto, S.; Saitho, T.; Shen, Q.; Toyoda, T.; Yoshino, K.; Pandey, S. S.; Ma, T.; Hayase, S. *J. Phys. Chem. C* **2014**, *118*, 16651.

(21) Neale, N. R.; Kopidakis, N.; van de Lagemaat, J.; Grätzel, M.; Frank, A. J. *J. Phys. Chem. B* **2005**, *109*, 23183.

(22) Bulliard, X.; Ihn, S.-G.; Yun, S.; Kim, Y.; Choi, D.; Choi, J.-Y.; Kim, M.; Sim, M.; Park, J.-H.; Choi, W.; Cho, K. *Adv. Funct. Mater.* **2010**, *20*, 4381.

(23) Goh, C.; Scully, S. R.; McGehee, M. D. *J. Appl. Phys.* **2007**, *101*, No. 114503.

(24) Zhao, Y.; Zhu, K. *J. Phys. Chem. Lett.* **2014**, *5*, 4175.

(25) Yin, W.-J.; Yang, J.-H.; Kang, J.; Yan, Y.; Wei, S.-H. *J. Mater. Chem. A* **2015**, DOI: 10.1039/c4ta05033a.

(26) Zhang, S.; Audebert, P.; Wei, Y.; Al Choueiry, A.; Lanty, G.; Bréhier, A.; Galmiche, L.; Clavier, G.; Boissière, C.; Lauret, J.-S.; Deleporte, E. *Materials* **2010**, *3*, 3385.

(27) Hsieh, S.-N.; Chen, S.-P.; Li, C.-Y.; Wen, T.-C.; Guo, T.-F.; Hsu, Y.-J. *Org. Electron.* **2009**, *10*, 1626.

(28) Guerrero, A.; Juarez-Perez, E. J.; Bisquert, J.; Mora-Sero, I.; Garcia-Belmonte, G. *Appl. Phys. Lett.* **2014**, *105*, No. 133902.